Identifying Quantitative *In Vivo* Multi-Parametric MRI Features For Treatment Related Changes after Laser Interstitial Thermal Therapy of Prostate Cancer

Satish Viswanath[a,*], **Robert Toth**[a,b], **Mirabela Rusu**[a], **Dan Sperling**[c], **Herbert Lepor**[d], **Jurgen Futterer**[e], and **Anant Madabhushi**[a,*]

[a]Case Western Reserve University, NJ, USA [b]Rutgers University, NJ, USA [c]Sperling Prostate Center, NY, USA [d]NYU Langone Medical Center, NY, USA [e]Radboud University Nijmegen Medical Centre, The Netherlands

Abstract

Laser interstitial thermal therapy (LITT) is a new therapeutic strategy being explored in prostate cancer (CaP), which involves focal ablation of organlocalized tumor via an interstitial laser fiber. While little is known about treatment-related changes following LITT, studying post-LITT changes via imaging is extremely significant for enabling early image-guided intervention and follow-up. In this work, we present the first attempt at examining focal treatment-related changes on a per-voxel basis via quantitative comparison of MRI features pre- and post-LITT, and hence identifying computerized MRI features that are highly sensitive as well as specific to post-LITT changes within the ablation zone in the prostate. A retrospective cohort of 5 patient datasets comprising both pre- and post-LITT T2-weighted (T2w) and diffusion-weighted (DWI) acquisitions was considered, where DWI MRI yielded an Apparent Diffusion Co-efficient (ADC) map. Our scheme involved (1) inter-protocol registration of T2w and ADC MRI, as well as inter-acquisition registration of pre- and post-LITT MRI, (2) quantitation of MRI parameters by correcting for intensity drift in order to examine tissuespecific response, and (3) quantification of the information captured by T2w MRI and ADC maps via texture and intensity features. Correction of parameter drift resulted in visually discernible improvements in highlighting tissue-specific response in different MRI features. Quantitative, voxel-wise comparison of the changes in different MRI features indicated that steerable and non-steerable gradient texture features, rather than the original T2w intensity and ADC values, were highly sensitive as well as specific in identifying changes within the ablation zone pre- and post-LITT. The highest ranked texture feature yielded a normalized percentage change of 186% within the ablation zone and 43% in a spatially distinct normal region, relative to its pre-LITT value. By comparison, both the original T2w intensity and ADC value demonstrated a markedly less sensitive and specific response to

*Corresponding Author: 10900 Euclid Ave, Wickenden 523D, Cleveland, OH 44118, USA. Tel: +1 (216) 368-3888. sev21@case.edu (Satish Viswanath), axm788@case.edu (Anant Madabhushi).

changes within the ablation zone. Qualitative as well as quantitative evaluation of co-occurrence texture features indicated the presence of LITT-related effects such as edema adjacent to the ablation zone, which were indiscernible on the original T2w and ADC images. Our preliminary results thus indicate great potential for non-invasive computerized MRI imaging features for determining focal treatment related changes, informing image-guided interventions, as well as predicting long- and short-term patient outcome.

Keywords

treatment evaluation; laser interstitial thermal therapy; prostate cancer; focal treatment; treatment change; registration; multi-parametric MRI

1. INTRODUCTION

Prostate cancer (CaP) is the most frequent malignancy diagnosed in men 50 years and older in industrialized countries[1]. However, while 1 in 6 men may be diagnosed with prostate cancer, only 1 in 36 will die from it[1]. There is thus an increasing clinical preference to put patients with more focal, lower grade CaP on active surveillance, where they are monitored for disease metastasis. Focal therapy options provide a useful adjunct to active surveillance, with significantly lower morbidity (urinary, sexual dysfunction)[2] compared to more radical treatment options (prostatectomy, radiation treatment). They additionally reduce the overtreatment of CaP in the general population, while allowing patients to have their disease treated once diagnosed[2].

Focal therapy strategies such as laser interstitial thermal therapy (LITT), high intensity focused ultrasound (HIFU), cryotherapy, and photo-dynamic therapy (PDT) are considered highly effective for targeting the *index lesion*, or the largest focus of CaP as measured by volume, within the prostate[3]. Most secondary (non-index) tumors tend to exhibit relatively smaller volumes and rarely have a higher Gleason score than the index lesion; making them unlikely to affect overall disease progression[4]. Thus, biologically speaking, most patients can be considered to have unifocal disease (i.e. the index lesion), by targeting which one can dramatically decrease total tumor volume and eliminate the most likely source of metastasis[5].

The specific focal therapeutic strategy considered in this work is LITT, which involves thermal destruction of tissue via the Nd-YAG laser delivered by an interstitial fiber. Heat energy is delivered to raise the temperature within the targeted CaP region, where rapid coagulative necrosis and instant cell death occur above 60° C. One of the major advantages enjoyed by LITT is its compatibility with magnetic resonance imaging (MRI), allowing for high resolution *in vivo* imaging to be used in LITT procedures[6]. MRI is also capable of monitoring temperature change in the tissue, which enables real-time monitoring of LITT. Further, multi-parametric MRI offers the ability to accurately denote the specific location of biopsy-proven CaP within the gland[1], which is very important for accurately delineating ablation zones within the prostate as well as for accurate guidance of the laser fiber during treatment.

In organs such as the liver, the extent of tissue necrosis due to LITT has been shown to be visible on MRI[7]. Rosenkrantz et al[6] have described some of the primary imaging characteristics at the 6-month follow-up mark after most types of focal therapy (though this study was not limited to LITT). The most significant of these was a decrease in the prostate volume (leading to loss of differentiation between prostatic zones), as well as poor visualization of the capsule. Structural T2w MRI is considered to be of limited utility to evaluate focal therapy effects due to presence of multifocal hypointensities that appear due to prostatic parenchyma[6], post-therapy. Diffusion weighted imaging (DWI) accurately visualizes tissue viability post-LITT (based on increased water diffusion), but its ability to differentiate between normal tissue, necrosis, and residual tumor has not been studied. Additionally, to our knowledge, the relative importance and utility of different MRI protocols in determining post-LITT effects has not been explored in detail.

There is thus relatively little information regarding the specific *in vivo* imaging characteristics of LITT-induced changes in the prostate. Further, the qualitative observations of LITT-related changes on prostate MP-MRI do not specifically address how to differentiate between the appearance of benign LITT-related changes (edema, necrosis) that can mask the presence of residual CaP, post-LITT. This implies a need for co-registration and image analysis methods to quantitatively compare pre- and post-LITT MRI in order to identify voxel-by-voxel changes inMRI parameters that can describe LITT-related changes within the prostate. Careful co-registration of pre- and post-LITT MRI can enable accurate overlays of the two acquisitions as well as voxel-wise comparison of the ablation zone (focally targeted index lesion) between pre- and post-LITT MRI acquisitions. Superposing the ablation zone from the pre-LITT MRI onto the post-LITT MRI can help identify imaging characteristics that correspond to residual disease (which would primarily occur within the ablation zone), as well as for benign LITT-related changes (edema, necrosis) that may appear external to the ablation zone.

In this work, we present the first attempt at quantitative image analysis of high-resolution (per-voxel) evaluation of treatment-related changes *in vivo* in CaP patients who have undergone LITT, via co-registration of preand post-LITT MRI acquisitions. Our approach is intended to form a precursor to building of a novel imaging-based predictor of early focal treatment response in CaP, to enable effective image-guided intervention. Our scheme may also find application in examining quantitative changes in non-invasive imaging markers as a function of time, to be correlated against long-term disease outcome and patient prognosis.

The remainder of this paper is organized as follows. Section 2 describes previous related work in quantitative treatment evaluation and Section 3 provides an overview of the methods used in the current work. Section 4 details the experimental design, while Section 5 summarizes the experimental results and discussion. Finally, Section 6 presents our concluding remarks.

2. PREVIOUS RELATED WORK

Treatment evaluation of therapeutic options for prostate cancer have primarily been examined for radiation treatment in a number of qualitative studies[8–12]. Our group[13,14] has

leveraged these qualitative characteristics within novel quantitative schemes for per-voxel evaluation and MRI signature construction to differentiate between possible radiation treatment outcomes (success, unsuccessful, recurrence). However, to our knowledge there is no similar work on evaluating treatment related changes due to LITT, via co-registration and quantitative analysis of pre- and post-LITT MRI.

MR thermometry measurements acquired during LITT have been utilized for predicting cell death using animal models[15–17]. These have involved construction of simulated mathematical models which can provide an estimate of cell death at a location, given the temporal thermometry information during treatment for that location and certain assumptions regarding temperature effects *in vivo*. Validation of these models has been done via rigid co-registration between thermometry images and post-LITT MRI[15] or histology[16,17], enabling comparison of actual regions of cell death against a simulated heatmap.

In studies involving prostate cancer patients, a Phase I LITT trial found good correlation between volumes of thermal damage that were visible on MRI and those determined via staining of *ex vivo* surgical prostatectomy specimens from patients who had previously undergone LITT[18]. Additionally while the ablated volume measured on MRI was marginally overestimated compared to pathology, MR images demonstrated excellent capability in discriminating non-viable necrotic tissue, post-ablation. More recently, co-registration approaches have been proposed for planning[19] and guidance[20] of LITT for prostate cancer using MRI information. These methods involved on the construction of a phantom to simulate focal treatment, as well as application of the simulated information for accurate targeting of focal treatment via fusion of MRI and ultrasound.

3. MOTIVATION AND BRIEF OVERVIEW

In this work, we present the first results of utilizing careful co-registration and image analytic tools to enable high-resolution (per-voxel) evaluation of treatment-related changes *in vivo* in CaP patients who have undergone LITT, using MRI information. A retrospective cohort of prostate MRI data that comprises both pre- and post-LITT acquisitions, including T2-weighted (T2w) and diffusion-weighted (DWI) protocols will be utilized, where an Apparent Diffusion Co-efficient (ADC) map is calculated from DWI MRI.

Step 1. Registration

A spatially constrained affine registration scheme[14,21] will be used to bring the T2w and ADC images into alignment within each of the pre- and post-LITT acquisitions, as well as to align the pre- and post-LITT acquisitions. This co-registration step is performed in order to correct for (a) voxel size, resolution differences, and calculation artifacts between the ADC map and the T2w MRI, and (b) acquisition differences between the pre- and post-LITT MRI acquisitions. Once co-registered, the multiparametric MRI information (T2w, ADC) can be integrated on a per-voxel basis, while the comparison of MRI parameters before and after LITT can also be performed on a per-voxel basis.

All coregistration procedures will utilize a spatially constrained normalized mutual information (NMI) similarity measure, due to its robustness to non-linear intensity relationships[21]. This particular registration methodology was chosen as it has been well-validated for different multi-modal registration applications[21]. This methodology has previously resulted in successful registrations in quantitative treatment evaluation schemes[13,14], and was therefore utilized in the current work instead of developing a more complex deformable scheme.

Step 2. Correction of MR parameter drift

After segmentation of the prostate ROI, pre- and post-LITT MR parameters (T2w intensity, ADC value) will be quantitated by correcting for intensity drift between acquisitions[22]. This will be done using co-registered image volumes output from Step 1. MR intensity non-standardness (or intensity drift) causes image intensity values to not have a fixed tissue-specific meaning within the same imaging protocol, the same body region, or even within the same patient[22]. Correction of this artifact is done in order to quantitatively compare the changes in MRI parameters between pre- and post-LITT acquisitions, while ensuring tissue specific meaning for the parameters being compared.

Step 3. Texture feature extraction

The T2w and ADC images will be quantified via raw intensity values as well as via computerized texture features[23,24]. These will be extracted from the co-registered, drift-corrected image volumes output from Step 2. Texture features have previously demonstrated high effectiveness in characterizing the prostate appearance in order to differentiate between regions as well as types of tumors within the prostate[23,25]. Here, texture features will be extracted in order to to examine their ability in specifically capturing LITT-related changes within the prostate.

Step 4. Quantifying imaging changes due to LITT

Normalized percent differences (relative to the pre-LITT values) will be calculated between the pre- and post-LITT MRI features. This measure is extracted in order to quantitatively evaluate the sensitivity and specificity of different MRI features in (1) detecting increased changes within the ablation zone as a result of LITT, while (2) demonstrating little to no change within a spatially distinct normal region. Evaluation of difference statistics will be limited to voxels within annotated, spatially distinct CaP and normal regions. By limiting the difference statistics calculations in this manner, false positive changes such as edema will not be taken into account when quantifying changes as a result of LITT.

Our methodology (summarized in Figure 1) is intended to provide a deeper understanding of imagingrelated changes due to LITT *in vivo*. These findings may later enable early image-guided intervention in cases of unsuccessful or incomplete treatment, as determined by an MRI-based signature of LITT-related changes.

4. EXPERIMENTAL DESIGN AND DETAILEDMETHODOLOGICAL DESCRIPTION

4.1. Data Description

A cohort of 5 patient studies was obtained from the Sperling Prostate Center, under an IRB-approved retrospective study protocol. Prior to initial MR imaging, all patients had been confirmed to have organ localized prostate cancer with Gleason scores between 6 and 7 (based on core-needle biopsies, no single core had > 50% involvement). Final treatment outcome for all 5 patients was determined as successful due to no local recurrence or residual CaP being discerned on follow-up (during the post-LITT MP-MRI exam), in addition to a reduction in PSA levels.

4.2. Annotations

Annotations of the ablation zone (CaP) as well as benign regions (normal) on the pre-LITT T2w MRI were obtained via an expert radiologist who delineated the ablation zone (AZ) by considering the MR image appearance of the AZ and the location of the needle during treatment.

Care was taken to ensure that the CaP and normal regions were spatially distinct and of approximately the same volume, based on visual observation of the AZ. Further, normal regions were annotated within the same prostatic region (central gland or peripheral zone) and on the same 2D axial sections as that of the CaP annotation.

Additionally, the prostate capsule was segmented out on the pre-LITT T2w MRI by an expert radiologist.

4.3. Pre- and post-LITT MP-MRI acquisition

For each patient, pre- and post-LITT MP-MRI scans included T2w and DWI protocols. All studies were performed using a Siemens Symphony 1.5 Tesla MRI machine together with a whole-body coil for excitation, as well as a pelvic phase array coil for signal reception. Table 1 summarizes the protocol details for both pre- and post-LITT MRI acquisitions.

Each patient underwent an MRI-guided LITT procedure using the Visualase Thermal Therapy System (Visualase Inc, Houston, TX) between 1 and 4 months after the initial MP-MRI acquisition. This system comprised a surgical diode laser, a fiber-optic laser applicator with diffusing tip and a coaxial cooling catheter, a cooling circulation pump, and a computer workstation for processing and display of MR thermometry images. During LITT, laser applicator placement was performed using the Invivo DynaTRIM transrectal biopsy guidance system (Invivo, Pewaukee, WI). The post-LITT MP-MRI (T2w, DWI) scan was acquired for each patient between 3 and 4 months after the LITT procedure.

4.4. Notation

We define $\mathscr{C}_\beta^{pre} = (C, f_\beta^{pre})$ as the pre-LITT MR scene, where $\beta = \{t2w, adc\}$ corresponds to the different MR protocols, and $f_\beta^{pre}(c)$ is the T2w or ADC value associated with every

voxel c in a 3D grid C. $\mathscr{C}_{\beta}^{post}$ are the corresponding post-LITT MR scenes for T2w and ADC that have been aligned to $\mathscr{C}_{\beta}^{pre}$ (see Sections 4.5 and 4.6 for details). Note that any image scene $\mathscr{C}$ prior to undergoing registration is denoted via $\hat{\mathscr{C}}$ in Sections 4.5 and 4.6. For ease of notation, applying a transformation $\mathbf{T}$ to the image scene $\mathscr{C}$ will be denoted as,

$$\mathbf{T}(\mathscr{C}) = \{C, f(\mathbf{T}(c))\}. \quad (1)$$

The region annotated as the ablation zone (CaP) is denoted $A(C)$ while the normal, benign annotation is denoted $N(C)$.

4.5. Alignment of pre-, post-LITT T2w MRI

Post- to pre-LITT registration was performed using the T2w protocol as it visualizes internal prostatic structures with excellent resolution, enabling accurate image registration. The original MR volume was cropped to contain the prostate alone, and NMI was calculated within this area. A 3D affine transformation of $\hat{\mathscr{C}}_{t2w}^{post}$ onto $\mathscr{C}_{t2w}^{pre}$ was calculated, encompassing 12 degrees of freedom which encode image rotation, translation, shearing, and scale. As a result of registration, the aligned post-LITT T2w MRI scene was obtained as,

$$\mathscr{C}_{t2w}^{post} = \mathbf{T}^{pp}(\hat{\mathscr{C}}_{t2w}^{post}), \quad (2)$$

where $\mathbf{T}^{pp}$ represents applying the 3D affine transformation transforming post-LITT T2w MRI to pre-LITT T2w MRI, to every voxel $c \in C$.

Figures 2(a) and (c) visualize the image registration result of $\hat{\mathscr{C}}_{t2w}^{post}$ and $\mathscr{C}_{t2w}^{pre}$ in the form of a checkerboard pattern, where alternating squares correspond to images from each of $\mathscr{C}_{t2w}^{pre}$ and $\mathscr{C}_{t2w}^{post}$ (for two different studies). The contiguity of structures corresponding to prostatic zones, zonal boundaries, and nodules within the prostate capsule (green outline) suggest a successful co-registration between the two different acquisitions, accounting for the major changes to the prostate region as a result of LITT[6], including acquisition-based differences, patient movement, and changes to the prostate appearance.

4.6. Inter-protocol alignment of T2w, DWI MRI

The pre-LITT ADC map was brought into spatial alignment with corresponding $\hat{\mathscr{C}}_{t2w}^{pre}$ via volumetric affine registration driven by a spatially constrained NMI measure (similar to Section 4.5), yielding,

$$\mathscr{C}_{adc}^{pre} = \mathbf{T}^{pre}(\tilde{\mathscr{C}}_{adc}^{pre}), \quad (3)$$

where $\mathbf{T}^{pre}$ represents applying the 3D affine transformation transforming pre-LITT ADC to pre-LITT T2w MRI, to every voxel $c \in C$.

The post-LITT ADC map undergoes a two-step registration process where it is first brought into alignment with $\hat{\mathscr{C}}_{t2w}^{post}$, followed by a second transformation to bring it into alignment with $\mathscr{C}_{t2w}^{pre}$, i.e.

$$\mathscr{C}_{adc}^{post} = \mathbf{T}^{pp}\mathbf{T}^{post}(\tilde{\mathscr{C}}_{adc}^{post}), \quad (4)$$

where $\mathbf{T}^{post}$ transforms post-LITT ADC to post-LITT T2w MRI, followed by $\mathbf{T}^{pp}$ to align it to the pre-LITT T2w MRI. All MRI data is thus transformed into the pre-LITT T2w MRI co-ordinate frame C and field of view (FOV, 512×512 voxels).

The final set of co-registered MRI protocols were visually inspected by an expert on a slice-by-slice basis for accuracy. The expert checked for anatomic contiguity, correct mapping of regions to one another, and overall accurate correspondence between internal prostatic structures between co-registered volumes. Figures 2(b) and (d) visualize the registration result of $\tilde{\mathscr{C}}_{adc}^{pre}$ to $\mathscr{C}_{t2w}^{pre}$ in the form of a checkerboard, where alternating squares correspond to images from each of $\mathscr{C}_{adc}^{pre}$ and $\mathscr{C}_{t2w}^{pre}$ (for two different studies). Similar to Figures 2(a) and (c), zonal boundaries and nodules within the prostate capsule (green outline) are seen to be contiguous between the two protocols, suggesting a successful registration accounting for voxel size and resolution differences between the 2 protocols.

4.7. Quantitation of pre- and post-LITT T2w and ADC values via correction of parameter drift between acquisitions

The MR acquisitions pre- and post-LITT were not found to suffer from MR bias field intensity inhomogeneity[27], most likely due to the use of a surface coil.

However, when the image intensity distributions for $\mathscr{C}_{t2}^{pre}$ (blue) and $\mathscr{C}_{t2}^{post}$ (red) were plotted together (Figure 3(a)), it was clear they were not in alignment, implying the presence of intensity drift (or non-standardness)[22] between the pre- and post-LITT acquisitions. A similar trend was observed when plotting the distributions for $\mathscr{C}_{adc}^{pre}$ (blue) and $\mathscr{C}_{adc}^{post}$ (red) (Figure 3(c), implying the presence of drift in ADC values between the two acquisitions.

The Nyul and Udupa algorithm[26] was implemented to automatically identify corresponding landmarks on these image intensity distributions, and non-linearly map them to one other. The mapping was calculated as a piece-wise linear transform between corresponding ranges on the intensity distributions of the two acquisitions. The intensity distributions were calculated within image regions local to the prostate capsule. Using the expert annotations, intensity values corresponding to prostate cancer were prevented from influencing the standardization procedure. As a result of intensity standardization, the distributions were aligned (Figures 3(b) and (d)) and the MR parameters could be directly compared. Intensity standardization was performed for corresponding pairs of protocols $(\mathscr{C}_{t2}^{post}/\mathscr{C}_{t2}^{pre}, \mathscr{C}_{adc}^{pre}/\mathscr{C}_{adc}^{post})$ between pre- and post-LITT MRI acquisitions.

The importance of correcting for intensity drift is further illustrated in Figures 3(e) – (h) where difference maps between pre- and post-LITT MRI protocols have been visualized

(see Section 4.9 for details). The difference maps calculated from non-standardized data (Figures 3(e) and (g)) which correspond to distributions exhibiting intensity drift (Figures 3(a) and (c)) clearly visualize a number of false positives outside the ablation zone (on the lower right). By contrast, difference maps calculated from standardized data (Figures 3(f) and (h) with corresponding aligned distributions in Figures 3(b) and (d)) have visibly fewer false positive areas outside the ablation zone. Thus, correcting for intensity drift enables a more quantitative comparison of MRI parameters between pre- and post-LITT acquisitions, with tissuespecific meaning for the imaging response.

The prostate capsule segmentation was applied to each of $\mathscr{C}_{t2w}^{pre}$, $\mathscr{C}_{t2w}^{post}$, $\mathscr{C}_{adc}^{pre}$, and $\mathscr{C}_{adc}^{post}$ in order to restrict all analysis to within the prostate region-of-interest alone.

4.8. Quantification of MRI information via texture features

A total of 78 texture features were extracted from each of $\mathscr{C}_{t2w}^{pre}$, $\mathscr{C}_{t2w}^{post}$, $\mathscr{C}_{adc}^{pre}$, and $\mathscr{C}_{adc}^{post}$ on a per-voxel basis (see Table 2). These features are obtained by (1) calculating responses to various filter operators, and (2) computing gray level intensity co-occurrence statistics, as follows,

1. *Non-steerable gradient features*: A set of 17 non-steerable gradient features were obtained via convolution with Sobel and Kirsch edge filters and first-order spatial derivative operators from each of $\mathscr{C}_{t2w}^{pre}$, $\mathscr{C}_{t2w}^{post}$, $\mathscr{C}_{adc}^{pre}$, and $\mathscr{C}_{adc}^{post}$. These operators allow for detection of the strength of horizontal, vertical, and diagonal edges within the image using linear kernels[28].

2. *Steerable gradient features*: Gabor operators comprise the steerable class of gradient calculations which attempt to match localized frequency characteristics[29]. A Gabor filter can be defined as the modulation of a complex sinusoid by a Gaussian function and is controlled by scale (λ) and orientation (θ) parameters. 48 Gabor features were extracted from each of $\mathscr{C}_{t2w}^{pre}$, $\mathscr{C}_{t2w}^{post}$, $\mathscr{C}_{adc}^{pre}$, and $\mathscr{C}_{adc}^{post}$ via convolution with distinct Gabor operators obtained by varying each of the associated parameters.

3. *Second order statistical features*: Second order statistical features have been proposed by Haralick[30] and have found wide application in computing features with perceptual meaning for computerized detection systems[23,24]. These features are based on quantifying the spatial gray-level co-occurrence within local neighborhoods around each pixel in an image, stored in the form of co-occurrence matrices. 13 Haralick features were calculated from each of $\mathscr{C}_{t2w}^{pre}$, $\mathscr{C}_{t2w}^{post}$, $\mathscr{C}_{adc}^{pre}$, and $\mathscr{C}_{adc}^{post}$, based on statistics derived from the corresponding co-occurrence matrices.

Feature extraction results in feature scenes $\mathscr{F}_{\varphi,\psi}^{\kappa} = (C, f_{\varphi,\psi}^{\kappa})$, where $f_{\varphi,\psi}^{\kappa}(c)$ is the feature value at location $c \in C$ when feature operator ϕ is applied to scene $\mathscr{C}_{\psi}^{\kappa}$, $\kappa \in \{pre, post\}$, $\psi \in \{t2w, adc\}$. For ease of notation, the raw T2w intensity value and ADC value were included in this set of feature scenes, i.e. there are a total of 79 feature scenes corresponding to each of $\mathscr{C}_{t2w}^{pre}$, $\mathscr{C}_{t2w}^{post}$, $\mathscr{C}_{adc}^{pre}$, and $\mathscr{C}_{adc}^{post}$.

4.9. Quantifying LITT-related changes in MRI features

For each of $\mathscr{F}_{\varphi,\psi}^{\kappa}$, $\phi \in \{1, \ldots, 79\}$, $\kappa \in \{pre, post\}$, $\psi \in \{t2w, adc\}$, the range of values was normalized to have a mean of 0 and a mean absolute deviation of 1. This ensured that the different parameter values were in a comparable range of values when quantifying differences between pre- and post-LITT MP-MRI.

The L_1 norm difference between a given pre- and post-LITT MP-MRI feature value can be calculated as

$$\delta_{\varphi,\psi}(c) = f_{\varphi,\psi}^{pre}(c) - f_{\varphi,\psi}^{post}(c), \quad (5)$$

for every voxel $c \in C$ (after normalization).

Difference scenes can be visualized within the prostate ROI by utilizing a colormap, such that blue corresponds to small difference values and red corresponds to areas of high differences. Therefore, regions annotated as $A(C)$ should be highlighted by red in the difference scene colormap, which would correspond to large changes within the ablation zone due to successful ablation of the CaP region. Along similar lines, regions annotated as $N(C)$ should be highlighted in blue in the difference scene colormap, corresponding to little to no change in a spatially distinct region not targeted by focal laser ablation. Note that this observation cannot be generalized to the entire prostate, as effects such as edema (among other reactions to treatment) may also cause significant changes to the MRI features[1,6].

The normalized percentage change each of $\mathscr{F}_{\varphi,\psi}^{post}$ with respect to the corresponding $\mathscr{F}_{\varphi,\psi}^{pre}$, $\phi \in \{1, \ldots, 79\}$, $\psi \in \{t2w, adc\}$ was calculated as,

$$\rho_{\varphi,\psi}^{A} = \text{MEDIAN}_{c \in A(C)} \frac{\delta_{\varphi,\psi}(c)}{f_{\varphi,\psi}^{pre}(c)}, \quad (6)$$

$$\rho_{\varphi,\psi}^{N} = \text{MEDIAN}_{c \in N(C)} \frac{\delta_{\varphi,\psi}(c)}{f_{\varphi,\psi}^{pre}(c)}. \quad (7)$$

$\rho_{\varphi,\psi}^{A}$ and $\rho_{\varphi,\psi}^{N}$ quantify the change in MP-MRI parameter ϕ within the annotated regions $N(C)$ and $A(C)$, and are implicitly normalized such that 0 corresponds to no difference between the pre- and post-LITT MRI feature, while values greater than 1 correspond to large differences. The median was utilized due to being less sensitive to outliers (unlike the mean), while not requiring rebinning of the data (unlike the mode).

In an ideal scenario, we would expect that $\rho_{\varphi,\psi}^{A}$ will be close to or greater than 1, corresponding to a large change in the MP-MRI feature ϕ within the successfully ablated CaP region (this would be considered a *highly sensitive* response). Similarly, $\rho_{\varphi,\psi}^{N}$ should ideally be close to 0, corresponding to no change in the MP-MRI feature ϕ within the normal region that should largely remain unaffected by focal ablation (implying a *highly specific* response).

Each MP-MRI feature was then ranked based on maximizing $\rho_{\varphi,\psi}^{A}$ while minimizing $\rho_{\varphi,\psi}^{N}$, ϕ $\in \{1, \ldots, 79\}$, $\psi \in \{t2w, adc\}$, via the scoring function

$$S(\rho_{\varphi,\psi})=(\rho_{\varphi,\psi}^{A})^{2} - (\rho_{\varphi,\psi}^{N})^{2}. \quad (8)$$

A high value for $S(\rho_{\phi,\psi})$ will correspond to a feature that is highly sensitive (i.e. $\rho_{\varphi,\psi}^{A}$ close to 1) as well as highly specific (i.e. $\rho_{\varphi,\psi}^{N}$ close to 0).

5. EXPERIMENTAL RESULTS AND DISCUSSION

5.1. Evaluating MP-MRI markers in quantifying LITT-related changes in vivo

Table 3 summarizes the top 20 T2w and ADC features, ranked in descending order, based on the scoring function $S(\rho)$. It can be observed that Gabor and Sobel features are the highest ranked features for accurately quantifying LITT-related changes within the prostate (i.e. high change within ablated region and low change within normal region). These texture features visualize responses across multiple scales, directions, and gradients, and are possibly quantifying changes in micro-architectural glandular orientation specifically occurring within the ablation zone, as a result of LITT.

Figure 4 visualizes a bar graph of $\rho_{\varphi,t2w}^{A}$ and $\rho_{\varphi,t2w}^{N}$ for each of the T2w features listed in Table 3, as well as for the raw T2w intensity value (not included in the top 20 features); together with the variance in these values overlaid as error bars. Figure 5 similarly visualizes trends for ADC features and the raw ADC value (included in the top 20 features), with corresponding error bars. The highest ranked ADC feature (Gabor $\theta = 1.18$, $\lambda = 45.25$) appears to be markedly more sensitive and specific in depicting changes due to LITT within the ablation zone relative to normal regions, compared to any other T2w or ADC feature considered.

A trend in $\rho_{\varphi,adc}^{A}$ and $\rho_{\varphi,adc}^{N}$ may be discerned in Figure 5 (seen in terms of bars with similar lengths) implying that highly ranked ADC features appear to have (1) relatively consistent change in each feature within ablated and non-ablated regions, and (2) markedly higher values for $\rho_{\varphi,adc}^{A}$ compared to $\rho_{\varphi,adc}^{N}$ demonstrating high sensitivity as well as specificity. By comparison, in Figure 4, the T2w features demonstrate more variability in the change in each feature (visualized as inconsistent lengths of bars). This variability can also be seen in the larger error bars in Figure 4. By comparison, Figure 5 illustrates that ADC features have lower variation (smaller error bars), as well as less variability in the change in each feature (consistent lengths of bars). Additionally, T2w features exhibit high values in $\rho_{\varphi,t2w}^{A}$ as well as in $\rho_{\varphi,t2w}^{N}$, implying a highly sensitive albeit less specific performance in quantifying LITT-related changes in the prostate.

The raw T2w intensity value did not rank in the top 20 T2w features in Table 3, and demonstrates higher $\rho_{1,t2w}^{N}$ than $\rho_{1,t2w}^{A}$ ($\phi = 1$ corresponds to the T2w intensity value), implying a relatively poor performance compared to any of the features listed in Table 3.

The raw ADC value, however, is ranked among the top 20 ADC features while demonstrating a markedly more sensitive as well as specific change between pre- and post-LITT acquisitions, compared to the T2w intensity value. For both protocols, derived texture features appear to provide a distinctly improved trade-off between sensitivity and specificity, by exhibiting a markedly increased change within cancerous regions compared to a markedly low change within benign regions.

5.2. Visualizing benign LITT-related changes via MRI features

Figure 6 compares the qualitative change in raw MRI parameters compared to derived texture features within $A(C)$ (red) and $N(C)$ (green). It is clear that the original T2w MRI (Figures 6(a) and (d)) do not show a distinct change within the CaP region, though the benign region has a reasonably consistent appearance. This is likely because diffuse T2w appearance is commonly observed after most types of treatment[6,9], causing confounders between the appearance of CaP and successfully treated CaP regions. The original ADC maps (Figures 6(b) and (e)) show a distinct brightening within the CaP region, but an inconsistent response within the benign region. The visualized ADC change within the CaP region may be explained by the fact that loss of cell membrane integrity (early process of cell death) and necrosis cause an increase in water mobility[31], which would result in an increase in the ADC value in that region.

A T2w texture feature (Haralick energy) was empirically selected as illustrative in terms of: (1) demonstrating a similar response pre- and post-LITT within $N(C)$ (green outline, low change), (2) illustrating different responses pre- and post-LITT within $A(C)$ (red outline, high change), as well as (3) visualizing tissue reaction to the LITT procedure as a distinct (over-expression) response that is adjacent to the AZ. Haralick energy attempts to quantify how heterogeneous the tissue appearance is and hence how smooth the variation in intensity values are. We have previously shown that such features demonstrate a response specific to peripheral zone tumors[23], which would explain why this feature demonstrates a distinct change after successful LITT ablation (due to absence of tumor post-LITT). Additionally, there appears to be a non-smooth variation in T2w intensities that is visually indiscernible in Figures 6(a), (d) but has been expressed by this feature, which may imply the presence of edema or a similar LITT-related change which may be expected to occur as a result of ablation[6].

The corresponding difference maps for these features: $\delta_{1,t2w}$ (T2w intensity), $\delta_{1,adc}$ (ADC value), $\delta_{18,t2w}$ (T2w Haralick energy), were quantitatively compared in terms of their spatial distribution over all studies considered (illustrated via box-and-whisker plots in Figure 7). The original MR parameters (T2w intensity, ADC value) depict only a marginal change in the difference values between the AZ and the region adjacent to the AZ. The Haralick energy feature (Figure 7(c)) appears to demonstrate the most distinct difference values between the two regions with the least overlap. This implies that LITT-related changes that are adjacent to the AZ (such as edema) may be associated with a distinct set of textural values compared to the changes occurring within AZ itself.

6. CONCLUDING REMARKS

Laser interstitial thermal therapy (LITT) is a highly promising focal strategy for low-grade, organ-confined prostate cancer, further enhanced by its ease of integration with high resolution MP-MR imaging. In order for LITT to gain popularity as a treatment strategy, it is important to be able to qualify and quantify LITT treatment response which can enable early image-guided intervention in patients where initial treatment was inaccurate or ineffective. In this work, we have presented preliminary results of evaluating treatment-related changes *in vivo* after LITT for prostate cancer patients. Our initial results based on 5 patient studies indicate that,

- Computerized textural descriptors derived from T2w and ADC images yielded distinctly more sensitive and specific responses, evaluated on a voxel-by-voxel basis, within regions of prostate cancer that were successfully ablated compared to normal regions (where the latter should ideally be unaffected by focal treatment).

- Sobel and Gabor responses, which comprise the steerable and nonsteerable class of texture features[28,29], were primarily ranked highest within each of the T2w and ADC feature sets, based on a scoring function that attempted to maximize percentage change within the ablation zone while minimizing change within a normal region (between pre- and post-LITT MRI features). This implies the presence of distinct micro-architectural orientation and gradient changes occurring specifically within the ablation zone as a result of LITT, possibly due to the presence of necrotic or ablated tissue in this region. However, normal regions show a markedly lower change in these features, likely because they are unaffected by the focal nature of LITT.

- Several empirically chosen T2w co-occurrence texture features[30] were found to be both sensitive and specific to visualizing (a) effects of successfully ablating the CaP regions, as well as (b) providing an indication of additional treatment related changes such as edema. These features also appeared to exhibit distinct quantitative difference values within the AZ, compared to a region locally bounding the AZ. These features quantify heterogeneity in the tissue appearance which likely enables characterization of subtle tissue changes occurring due to edema or inflammation of regions surrounding the ablation zone, as a result of LITT.

- The original ADC values demonstrated highly sensitive response to LITT-related changes *in vivo*, as they are able to capture the significant change in water permeability as a result of treatment[31]. However, this effect may be non-specific to the ablation zone alone, resulting in a lower specificity for the raw ADC values.

- The T2w MRI intensity value was inconsistent in demonstrating LITT-related change, in terms of not demonstrating a distinctly sensitive or specific response within the ablation zone. This may be due to the diffuse appearance of T2w MRI post-therapy, which has been observed in previous qualitative studies[2,6].

- Correction of parameter drift between different acquisitions[22] enabled a rigorous voxel-by-voxel quantitation and comparison of T2w and ADC values. Our results demonstrated that correcting for this artifact results in a visually obvious

improvement when comparing tissue specific response on *in vivo* imaging, due to the LITT procedure.

We do acknowledge some limitations of the current work. We utilized a relatively simple spatially constrained volumetric affine registration scheme to align pre- and post-LITTMRI, as well as align the different MRI protocols (T2w, ADC), rather than a more complex deformable scheme. While a comprehensive comparison of different registration methods was not performed, our choice of method resulted in relatively robust, well-aligned results. Additionally, a quantitative evaluation of the registration results could not be performed due to lack of annotations to be used as ground truth. However, the methodology used by us is based on well-validated previous work[13,14,21].

In future work, deformations caused by the interstitial fiber protruding into the prostate tissue could be better accounted for through biomechanical modeling. Once these deformations are subtracted out, we may be able to perform a more detailed study of the tissue changes due to LITT alone.

Future work will also involve validation of our findings on a larger cohort of data. We will also examine evaluation of the MRI imaging markers identified in this work to provide an indication of treatment response post-LITT, in order to enable early image-guided intervention for patients who were non-responsive to the initial treatment. Other applications of the MRI features developed in this work could be in the context of constructing an imaging-based predictor for patient prognosis and long-term patient outcome.

Acknowledgments

References

1. Colin P, Mordon S, Nevoux P, Marqa M, Ouzzane A, Puech P, Bozzini G, Leroux B, Villers A, Betrouni N. Focal laser ablation of prostate cancer: definition, needs, and future. Adv Urol 2012. 2012:589160.

2. Oto A, Sethi I, Karczmar G, McNichols R, Ivancevic MK, Stadler WM, Watson S, Eggener S. MR Imagingguided Focal Laser Ablation for Prostate Cancer: Phase I Trial. Radiology. 2013

3. Wise AM, Stamey TA, McNeal JE, Clayton JL. Morphologic and clinical significance of multifocal prostate cancers in radical prostatectomy specimens. Urology. 2002; 60:264–269. [PubMed: 12137824]

4. Eggener SE, Scardino PT, Carroll PR, Zelefsky MJ, Sartor O, Hricak H, Wheeler TM, Fine SW, Trachtenberg J, Rubin MA, Ohori M, Kuroiwa K, Rossignol M, Abenhaim L. Focal Therapy for Localized Prostate Cancer: A Critical Appraisal of Rationale and Modalities. The Journal of Urology. 2007; 178:2260–2267. [PubMed: 17936815]

5. Ahmed HU. The Index Lesion and the Origin of Prostate Cancer. New England Journal of Medicine. 2009; 361:1704–1706. [PubMed: 19846858]

6. Rosenkrantz A, Scionti S, Mendrinos S, Taneja S. Role of MRI in minimally invasive focal ablative therapy for prostate cancer. AJR Am J Roentgenol. 2011; 197:W90–W96. [PubMed: 21701001]

7. Roberts HR, Paley M, Hall-Craggs MA, Lees WR, Friedman EP, Clemence M, Buonacorssi G, Bown SG. Dynamic magnetic resonance control of interstitial laser photocoagulation therapy of colorectal hepatic metastases. Lancet. 1994; 343:1221. [PubMed: 7909879]

8. Song I, Kim C, Park B, Park W. Assessment of Response to Radiotherapy for Prostate Cancer: Value of Diffusion-Weighted MRI at 3 T. Am. J. Roentgenol. 2010; 194:W477–W482. [PubMed: 20489065]

9. Westphalen A, Kurhanewicz J, Cunha R, Hsu I, Kornak J, Zhao S, Coakley F. T2-Weighted endorectal magnetic resonance imaging of prostate cancer after external beam radiation therapy. Int Braz J Urol. 2009; 35(2):171–180. [PubMed: 19409121]

10. Pucar D, Sella T, Schoder H. The role of imaging in the detection of prostate cancer local recurrence after radiation therapy and surgery. Curr Opin Urol. 2008; 18(1):87–97. [PubMed: 18090496]

11. Pickett B, Kurhanewicz J, Coakley F, Shinohara K, Fein B, Roach M. Use of MRI and spectroscopy in evaluation of external beam radiotherapy for prostate cancer. Int J Radiat Oncol Biol Phys. 2004; 60(4):1047–1055. [PubMed: 15519774]

12. Coakley F, Teh H, Qayyum A, Swanson M, Lu Y, Roach M, Pickett B, Shinohara K, Vigneron D, Kurhanewicz J. Endorectal MR imaging and MR spectroscopic imaging for locally recurrent prostate cancer after external beam radiation therapy: preliminary experience. Radiology. 2004; 233:441–448. [PubMed: 15375223]

13. Tiwari P, Viswanath S, Kurhanewicz J, Madabhushi A. Weighted Combination of Multi-Parametric MR Imaging Markers for Evaluating Radiation Therapy Related Changes in the Prostate. Workshop on Prostate Cancer Imaging (in conjunction with MICCAI). 2011; 6963:80–91.

14. Viswanath, S.; Tiwari, P.; Chappelow, J.; Toth, R.; Kurhanewicz, J.; Madabhushi, A. CADOnc: An integrated toolkit for evaluating radiation therapy related changes in the prostate using multiparametric MRI. Biomedical Imaging: From Nano to Macro; IEEE International Symposium on, 2011; 2011. p. 2095-2098.

15. Breen MS, Breen M, Butts K, Chen L, Saidel GM, Wilson DL. MRI-guided thermal ablation therapy: model and parameter estimates to predict cell death from MR thermometry images. Ann Biomed Eng. 2007; 35:1391–1403. [PubMed: 17436111]

16. Marqa MF, Colin P, Nevoux P, Mordon SR, Betrouni N. Focal laser ablation of prostate cancer: numerical simulation of temperature and damage distribution. Biomed Eng Online. 2011; 10:45. [PubMed: 21635775]

17. Bhowmick S, Swanlund DJ, Coad JE, Lulloff L, Hoey MF, Bischof JC. Evaluation of thermal therapy in a prostate cancer model using a wet electrode radiofrequency probe. J Endourol. 2001; 15:629–640. [PubMed: 11552790]

18. Lindner U, Lawrentschuk N, Weersink RA, Davidson SR, Raz O, Hlasny E, Langer DL, Gertner MR, Van der Kwast T, Haider MA, Trachtenberg J. Focal laser ablation for prostate cancer followed by radical prostatectomy: validation of focal therapy and imaging accuracy. Eur Urol. 2010; 57:1111–1114. [PubMed: 20346578]

19. Betrouni N, Nevoux P, Leroux B, Colin P, Puech P, Mordon S. An anatomically realistic and adaptable prostate phantom for laser thermotherapy treatment planning. Med Phys. 2013; 40:022701. [PubMed: 23387771]

20. Makni N, Puech P, Colin P, Azzouzi A, Mordon S, Betrouni N. Elastic image registration for guiding focal laser ablation of prostate cancer: preliminary results. Comput Methods Programs Biomed. 2012; 108:213–223. [PubMed: 22575803]

21. Chappelow J, Bloch BN, Rofsky N, Genega E, Lenkinski R, De-Wolf W, Madabhushi A. Elastic registration of multimodal prostate MRI and histology via multiattribute combined mutual information. Med Phys. 2011; 38:2005–2018. [PubMed: 21626933]

22. Madabhushi A, Udupa JK. New methods of MR image intensity standardization via generalized scale. Medical Physics. 2006; 33:3426–3434. [PubMed: 17022239]

23. Viswanath S, Bloch N, Chappelow J, Toth R, Rofsky N, Genega E, Lenkinski R, Madabhushi A. Central gland and peripheral zone prostate tumors have significantly different quantitative imaging

signatures on 3 Tesla endorectal, in vivo T2-weighted MR imagery. J Magn Reson Imaging. 2012; 36:213–224. [PubMed: 22337003]

24. Madabhushi A, Feldman MD, Metaxas DN, Tomaszeweski J, Chute D. Automated detection of prostatic adenocarcinoma from high-resolution ex vivo MRI. IEEE Trans Med Imaging. 2005; 24:1611–1625. [PubMed: 16350920]

25. Lopes R, Ayache A, Makni N, Puech P, Villers A, Mordon S, Betrouni N. Prostate cancer characterization on MR images using fractal features. Med Phys. 2010; 38:83–95. [PubMed: 21361178]

26. Nyul L, Udupa J, Zhang X. New variants of a method of mri scale standardization, Medical Imaging. IEEE Transactions on. 2000; 19:143–150.

27. Viswanath S, Palumbo D, Chappelow J, Patel P, Bloch BN, Rofsky N, Lenkinski R, Genega E, Madabhushi A. Empirical evaluation of bias field correction algorithms for computer-aided detection of prostate cancer on T2w MRI. SPIE Medical Imaging. 2011; 79630:79630V–79630V–12.

28. Agner SC, Soman S, Libfeld E, McDonald M, Thomas K, Englander S, Rosen MA, Chin D, Nosher J, Madabhushi A. Textural Kinetics: A Novel Dynamic Contrast-Enhanced (DCE)-MRI Feature for Breast Lesion Classification. J Digit Imaging. 2010; 24:446–463. [PubMed: 20508965]

29. Wang Y, Chua C-S. Face recognition from 2D and 3D images using 3D Gabor filters. Image and Vision Computing. 2005; 23(11):1018–1028.

30. Haralick RM, Shanmugam K, Dinstein I. Textural Features for Image Classification. IEEE Trans Sys Man Cybernetics. 1973; 3(6):610–621.

31. Pickles MD, Gibbs P, Lowry M, Turnbull LW. Diffusion changes precede size reduction in neoadjuvant treatment of breast cancer. Magnetic Resonance Imaging. 2006; 24:843–847. [PubMed: 16916701]
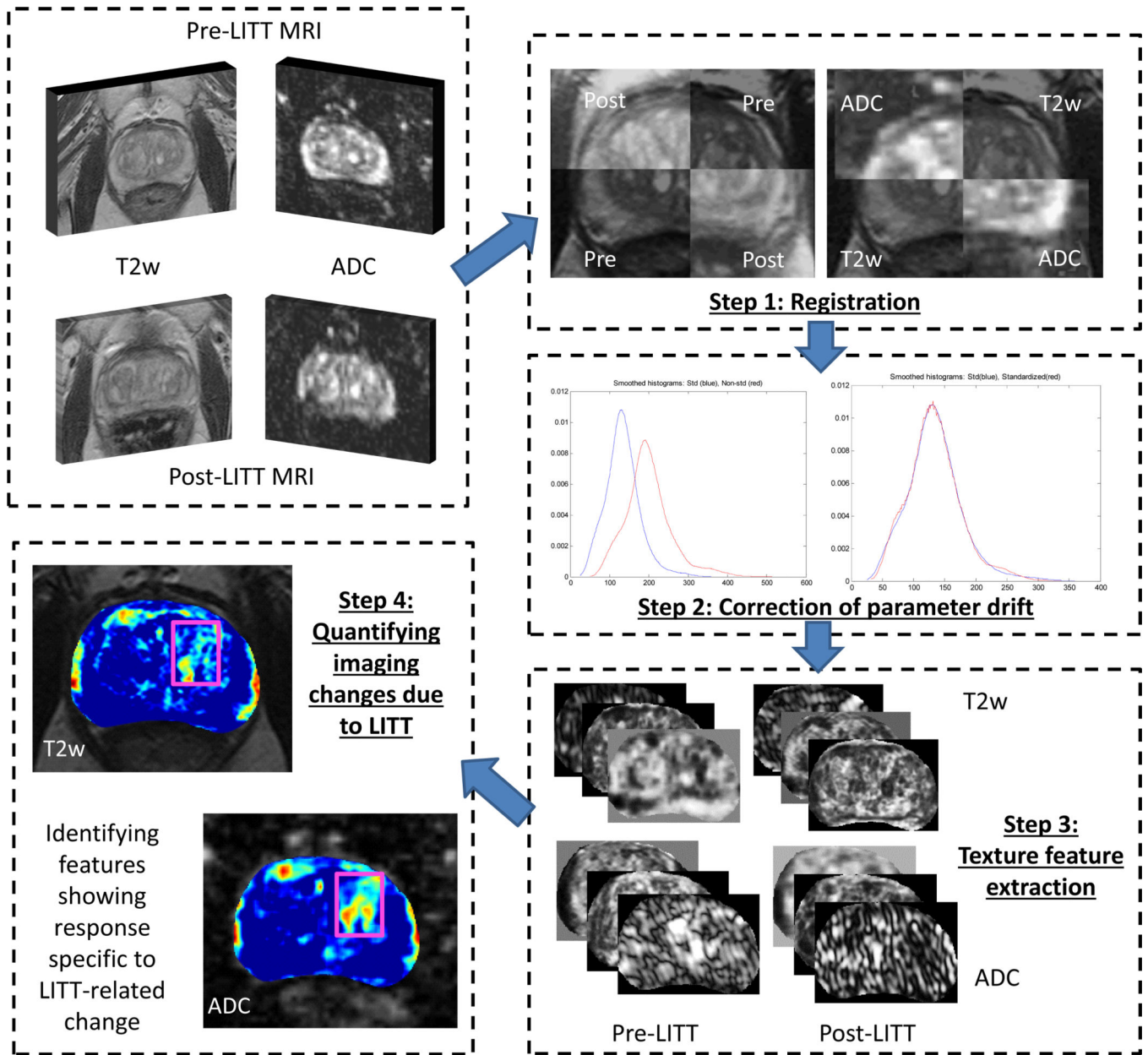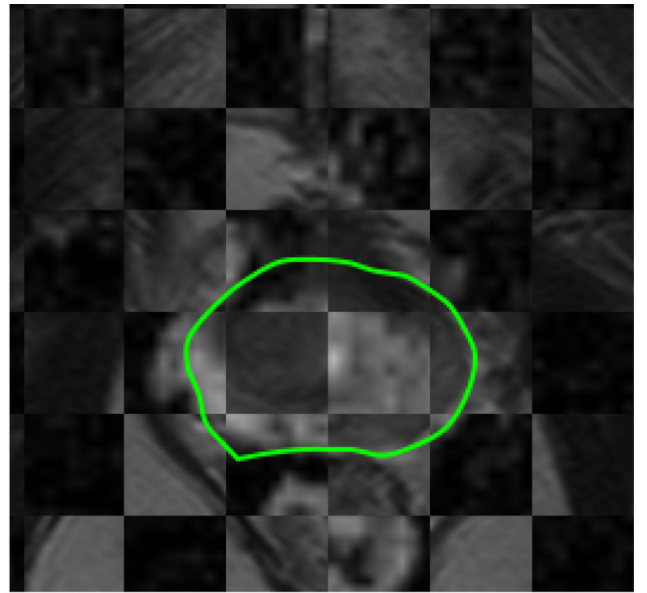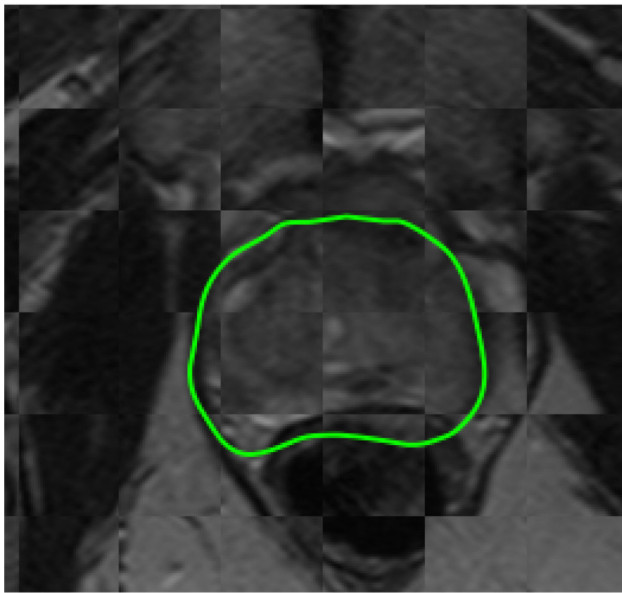
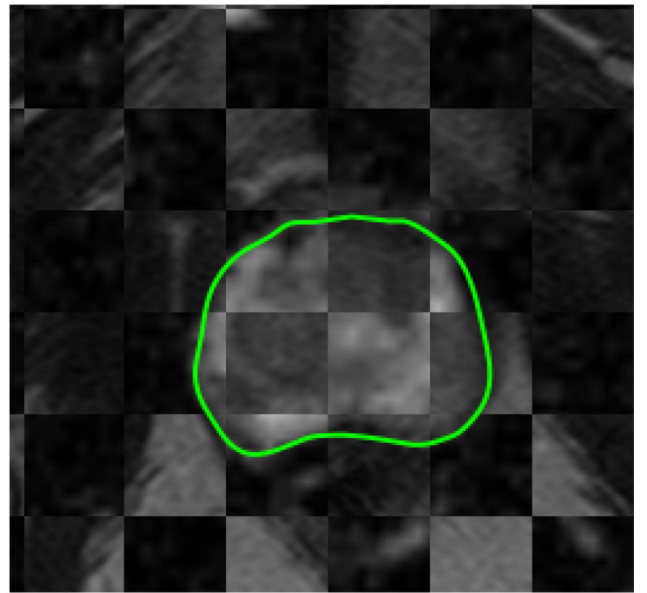**Figure 1.**
Overview of the methodology and overall workflow.
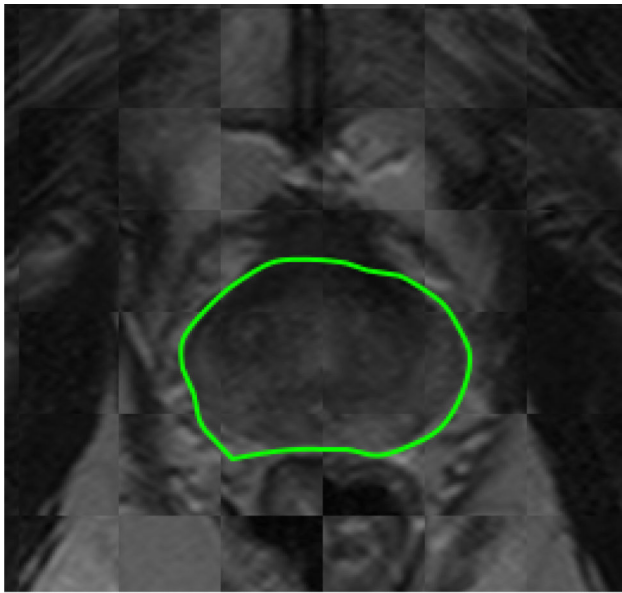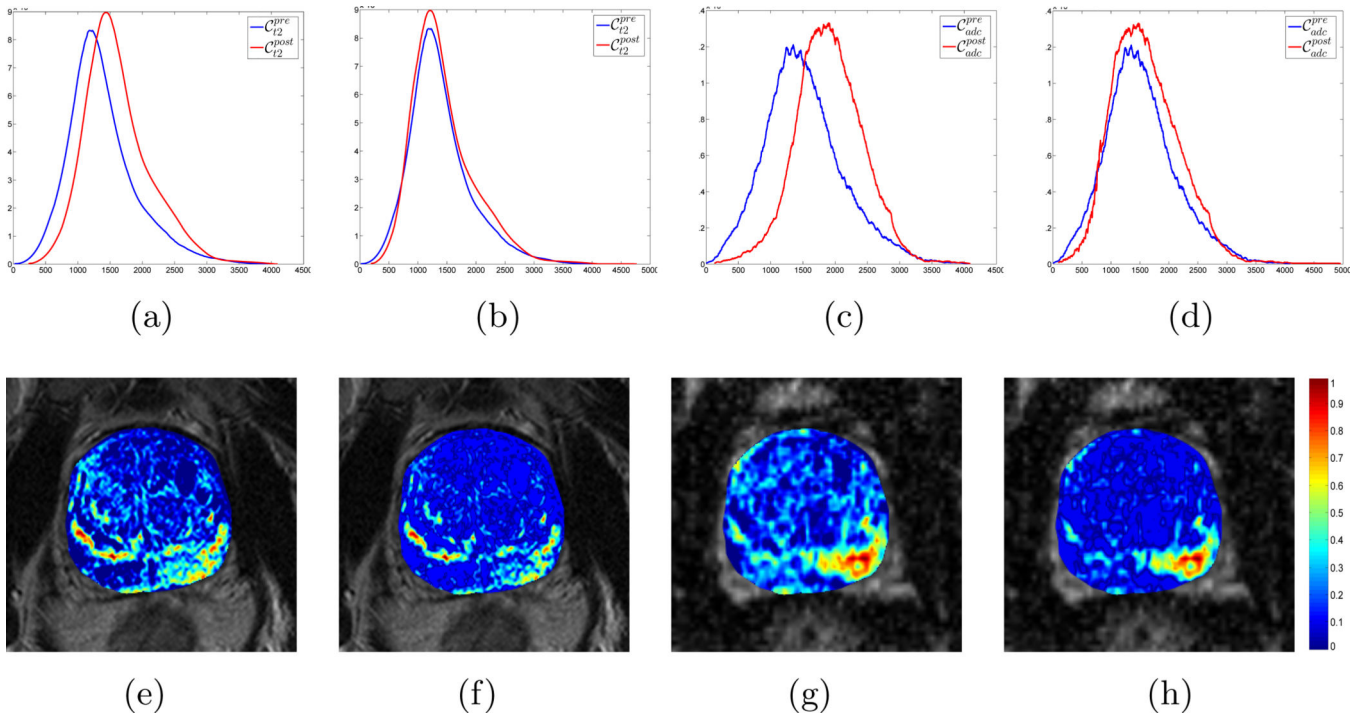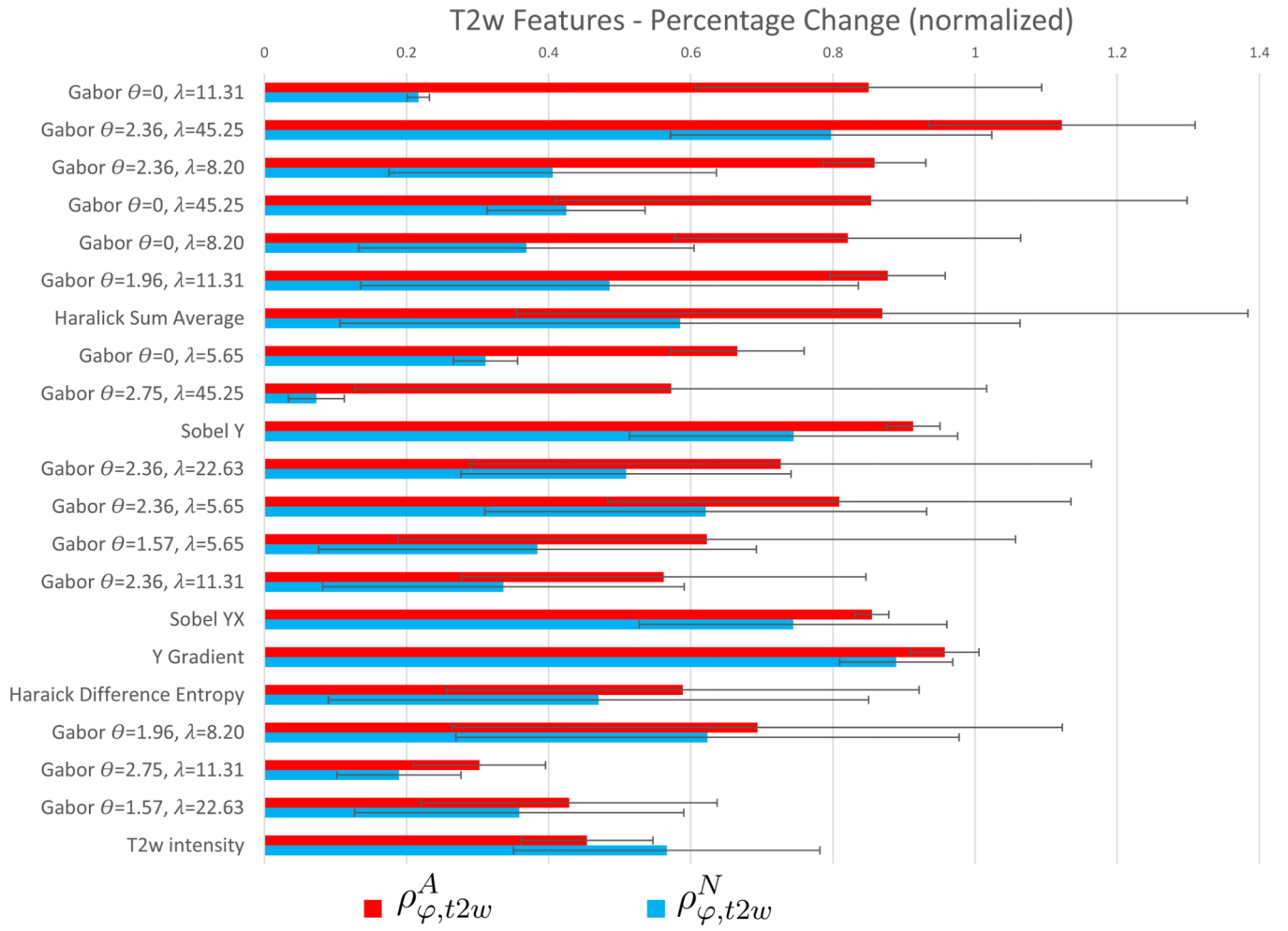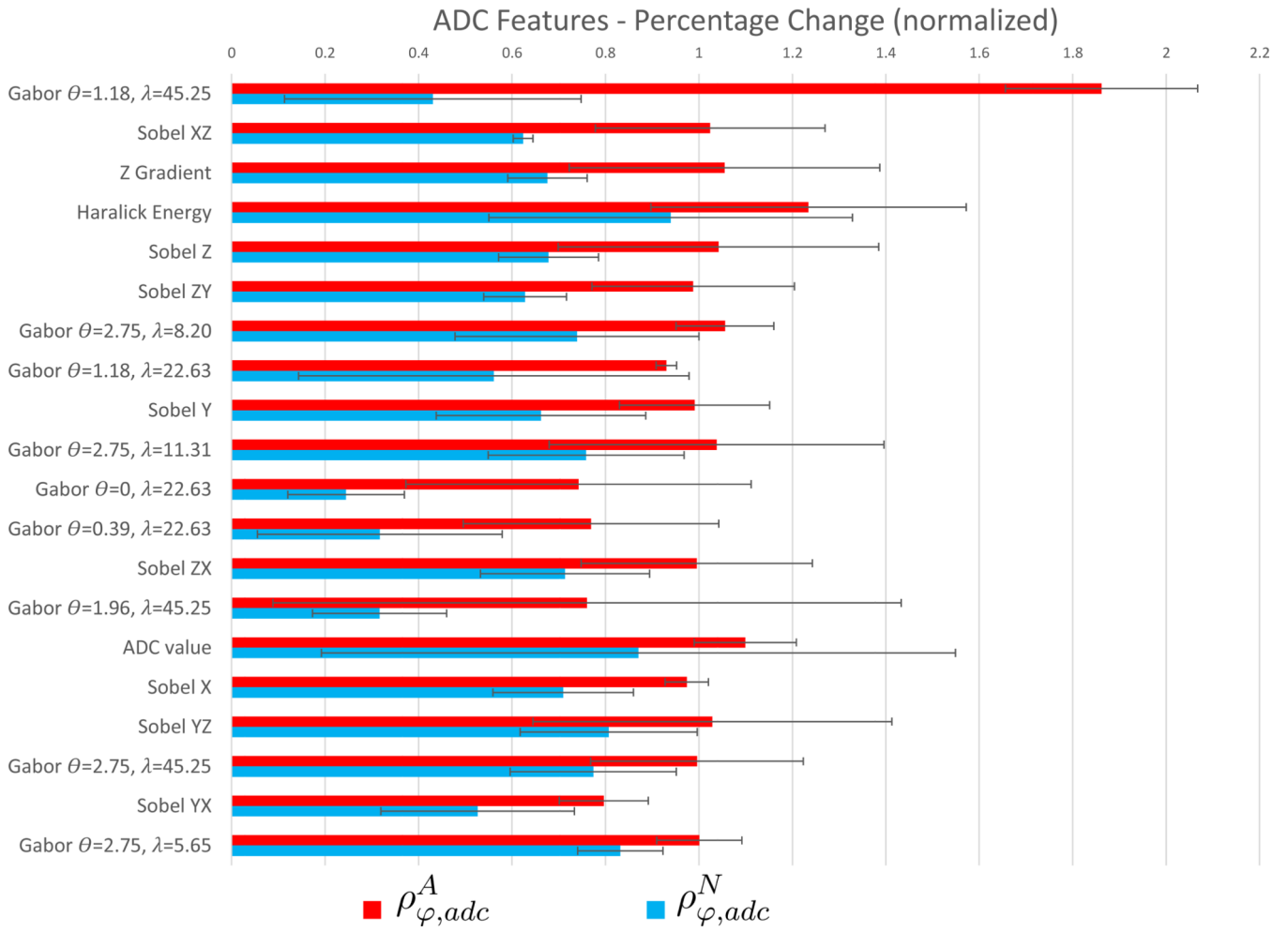
Figure 2.
Checkerboard overlays showing volumetric affine registration results (each row corresponds to a different patient study), (a),(c) $\mathscr{C}_{t2}^{post}/\mathscr{C}_{t2}^{pre}$ and (b),(d) $\mathscr{C}_{adc}^{pre}/\mathscr{C}_{t2}^{pre}$. Green outlines correspond to the prostate capsule segmentation (obtained via expert annotation of the T2w MRI). Note contiguous structures in each of these checkerboards denoting successful co-registration using affine registration, implying that more complex deformable registration procedure was not necessary in these cases.
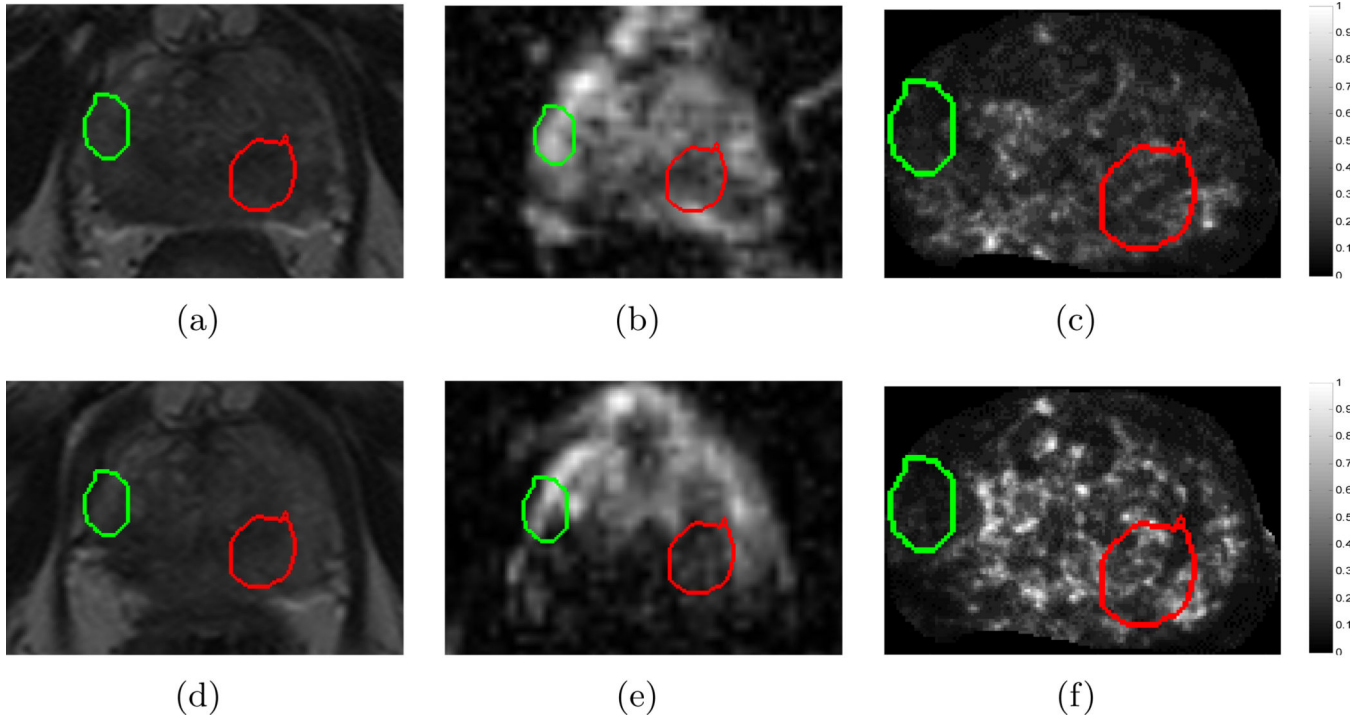
Figure 3.
Visualizing intensity drift between pre- (blue) and post-LITT (red) MR parameters in (a) T2w, and (c) ADC values, by plotting the corresponding distributions along the same axis. Note that after intensity standardization26, both the (b) T2w and (d) ADC distributions are no longer misaligned, implying successful correction of the drift artifact. This enables tissue-specific meaning when comparing MR parameter values between the two acquisitions. This is visualized via difference maps for (f) T2w intensity and (h) ADC values which exhibit markedly few positives outside the ablation zone on the lower right. By comparison, difference maps for (e) T2w intensity and (g) ADC values that have not been corrected for intensity drift exhibit a large number of false positives, implying a non-tissue specific response in imaging features for evaluating LITT-related changes inside and outside the ablation zone.

Figure 4.

Summary of $\rho_{\varphi,t2w}^{A}$ and $\rho_{\varphi,t2w}^{N}$ for the features in Table 3.

Figure 5.

Summary of $\rho_{\varphi,adc}^{A}$ and $\rho_{\varphi,adc}^{N}$ for the features in Table 3.

Figure 6.

Images from a single dataset corresponding to representative sections from (a) $\mathscr{C}_{t2w}^{pre}$, (d) $\mathscr{C}_{t2w}^{post}$, (b) $\mathscr{C}_{adc}^{pre}$, (e) $\mathscr{C}_{adc}^{post}$, (c) $\mathscr{F}_{t2w,20}^{pre}$, (f) $\mathscr{F}_{t2w,20}^{post}$. Green outlines correspond to benign regions ($N(C)$) while red outlines correspond to cancerous regions ($A(C)$), as annotated by a radiologist. While little change is observed within the CaP region (red) between (a) and (d) on T2w MRI, corresponding ADC value appears to change distinctly between (b) and (e). By contrast, an empirically chosen T2w feature (Haralick energy) illustrates distinct change within the CaP region (red), low change within benign region (green), as well as a reaction to LITT adjacent to $A(C)$, depicted via brighter values around the red outline (compare (c) and (f)).
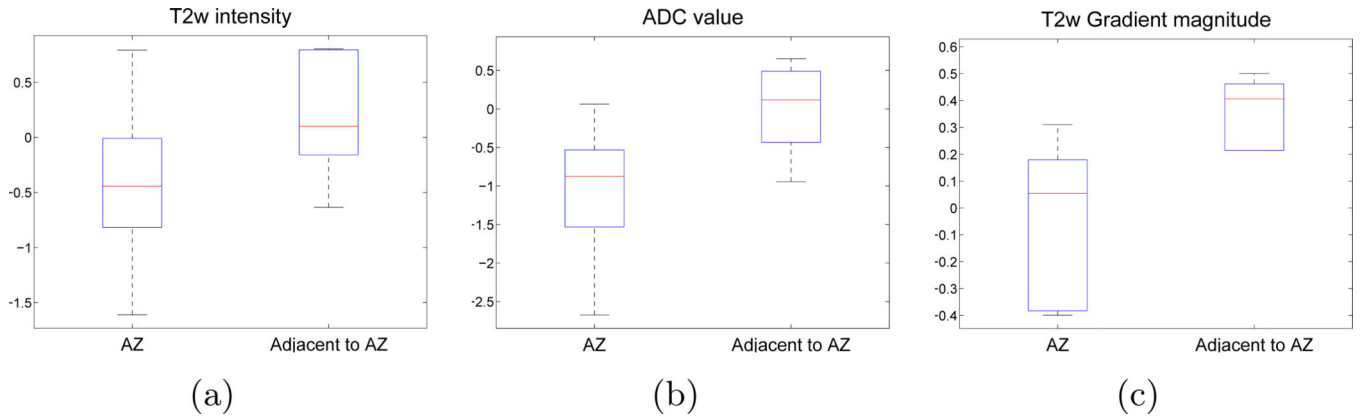
Figure 7.
Box-and-whisker plots (over all studies) depicting range of (a) $\delta_{1,t2w}$ (T2w signal intensity), (b), $\delta_{1,adc}$ (ADC value), and (c) $\delta_{18,t2w}$ (T2w Haralick energy); within the AZ and within a bounding box local to the AZ. Note that the red line in the middle of each box reflects the median difference value while the box is bounded by 25th and 75th percentile of difference values. The whisker plot extends to the minimum and maximum difference values outside the box. The derived T2w texture feature ((c)) expresses a markedly distinct difference signature within the AZ compared to the region adjacent to the AZ (with minimal overlap), as opposed to the original T2w and ADC parameters which do not.

Table 1

T2w and DWI acquisition parameters for pre- and post-LITT MRI exams.

Parameters	T2w	DWI
Directions	Axial	Axial
Sequence	Fast spin-echo	DTI-EPI
Field of view	14 cm	24 cm
Matrix size	256×192	256×128
Resolution	512×512	128×128 to 152×152
Other	TR/TE = 4000–6000/90–120, echo train length = 8–16, slice thickness = 3 mm, interslice gap = 0 mm	6 gradient directions b-values = {0, 600}, slice thickness = 4 mm

Table 2

Summary of parameters for texture features used (numbers in brackets signify how many features of each texture category were computed)

Feature	Parameters
Non-steerable gradient (17)	Sobel/Kirsch X,Y,Z and diagonal directions, gradient X,Y,Z directions and magnitude, 1st order statistics
Steerable gradient (48)	$\lambda = \{2.82, 5.66, 8.2, 11.31, 22.63, 45.25\}$ $\left(\dfrac{2^{2\ldots6}}{\sqrt{2}}\right)$ $\theta = \{0, 0.39, 0.78, 1.18, 1.57, 1.96, 2.36, 2.75\}$ $\left(0 \ldots 7 \times \dfrac{\pi}{8}\right)$
Second order statistical (13)	Entropy, energy, inertia, inverse difference moment, correlation, 2 information measures, sum average, sum variance, sum entropy, difference average, difference variance, difference entropy

Table 3

Top 20 T2w and ADC features, ranked in descending order based on $S(\rho)$, i.e. showing a high change within CaP (ablated) regions and a low change within normal regions.

Rank	T2w feature	ADC feature
1	Gabor $\theta=0$, $\lambda=11.31$	Gabor $\theta=1.18$, $\lambda=45.25$
2	Gabor $\theta=2.36$, $\lambda=45.25$	Sobel XZ
3	Gabor $\theta=2.36$, $\lambda=8.20$	Z Gradient
4	Gabor $\theta=0$, $\lambda=45.25$	Haralick Energy
5	Gabor $\theta=0$, $\lambda=8.20$	Sobel Z
6	Gabor $\theta=1.96$, $\lambda=11.31$	Sobel ZY
7	Haralick Sum Average	Gabor $\theta=2.75$, $\lambda=8.20$
8	Gabor $\theta=0$, $\lambda=5.65$	Gabor $\theta=1.18$, $\lambda=22.63$
9	Gabor $\theta=2.75$, $\lambda=45.25$	Sobel Y
10	Sobel Y	Gabor $\theta=2.75$, $\lambda=11.31$
11	Gabor $\theta=2.36$, $\lambda=22.63$	Gabor $\theta=0$, $\lambda=22.63$
12	Gabor $\theta=2.36$, $\lambda=5.65$	Gabor $\theta=0.39$, $\lambda=22.63$
13	Gabor $\theta=1.57$, $\lambda=5.65$	Sobel ZX
14	Gabor $\theta=2.36$, $\lambda=11.31$	Gabor $\theta=1.96$, $\lambda=45.25$
15	Sobel YX	ADC value
16	YGradient	Sobel X
17	Haralick Difference Entropy	Sobel YZ
18	Gabor $\theta=1.96$, $\lambda=8.20$	Gabor $\theta=2.75$, $\lambda=45.25$
19	Gabor $\theta=2.75$, $\lambda=11.31$	Sobel YX
20	Gabor $\theta=1.57$, $\lambda=22.63$	Gabor $\theta=2.75$, $\lambda=5.65$